IOPscience iopscience.iop.org

Home Search Collections Journals About Contact us My IOPscience

First-principles quantum molecular dynamics study of $Ti_xZr_{1-x}N(111)/SiN_y$ heterostructures and comparison with experimental results

This content has been downloaded from IOPscience. Please scroll down to see the full text.

2014 Sci. Technol. Adv. Mater. 15 025007

(http://iopscience.iop.org/1468-6996/15/2/025007)

View the table of contents for this issue, or go to the journal homepage for more

Download details:

IP Address: 31.135.144.241
This content was downloaded on 18/05/2014 at 19:45

Please note that terms and conditions apply.

OPEN ACCESS
IOP Publishing | National Institute for Materials Science
Science and Technology of Advanced Materials
Sci. Technol. Adv. Mater. **15** (2014) 025007 (11pp)
doi:10.1088/1468-6996/15/2/025007

First-principles quantum molecular dynamics study of $Ti_xZr_{1-x}N(111)/SiN_y$ heterostructures and comparison with experimental results

Volodymyr Ivashchenko[1], **Stan Veprek**[2], **Alexander Pogrebnjak**[3] **and Bogdan Postolnyi**[3]

[1] Institute of Problems of Material Science, NAS of Ukraine, Krzhyzhanovsky Street 3, 03142 Kyiv, Ukraine
[2] Department of Chemistry, Technical University Munich, Lichtenbergstrasse 4, D-85747 Garching, Germany
[3] Sumy State University, Rymsky-Korsakov Street 2, 40007 Sumy, Ukraine

E-mail: alexp@i.ua

Received 7 October 2013
Accepted for publication 16 January 2014
Published 30 April 2014

Abstract

The heterostructures of five monolayers B1–$Ti_xZr_{1-x}N(111)$, $x = 1.0$, 0.6, 0.4 and 0.0 (where B1 is a NaCl-type structure) with one monolayer of a Si_3N_4-like Si_2N_3 interfacial layer were investigated by means of first-principles quantum molecular dynamics and a structure optimization procedure using the Quantum ESPRESSO code. Slabs consisting of stoichiometric TiN and ZrN and random, as well as segregated, B1–$Ti_xZr_{1-x}N(111)$ solutions were considered. The calculations of the B1–$Ti_xZr_{1-x}N$ solid solutions, as well as of the heterostructures, showed that the pseudo-binary TiN–ZrN system exhibits a miscibility gap. The segregated heterostructures in which Zr atoms surround the Si_yN_z interface were found to be the most stable. For the Zr-rich heterostructures, the total energy of the random solid solution was lower compared to that of the segregated one, whereas for the Ti-rich heterostructures the opposite tendency was observed. Hard and super hard Zr–Ti–Si–N coatings with thicknesses from 2.8 to 3.5 μm were obtained using a vacuum arc source with high frequency stimulation. The samples were annealed in a vacuum and in air at 1200 °C. Experimental investigations of Zr–Ti–N, Zr–Ti–Si–N and Ti–Si–N coatings with different Zr, Ti and Si concentrations were carried out for comparison with results obtained from $Ti_xZr_{1-x}N(111)/SiN_y$ systems. During annealing, the hardness of the best series samples was increased from (39.6 ± 1.4) to 53.6 GPa, which seemed to indicate that a spinodal segregation along grain interfaces was finished. A maximum hardness of 40.8 GPa before and 55 GPa after annealing in air at 500 °C was observed for coatings with a concentration of elements of Si $\geqslant$ (7–8) at.%, Ti $\geqslant$ 22 at.% and Zr $\leqslant$ 70 at.%.

Keywords: Ti–Zr–N/SiN_x nanolayered coatings, interface, first-principles investigation, quantum molecular dynamics, superhard, nanocomposite, nanograins, compressive stress

Content from this work may be used under the terms of the Creative Commons Attribution-NonCommercial-ShareAlike 3.0 licence. Any further distribution of this work must maintain attribution to the author(s) and the title of the work, journal citation and DOI.

 © 2014 National Institute for Materials Science

1. Introduction

The superhard nanocomposites and nanolayered heterostructures exhibit an enhanced hardness of 40–100 and $\leqslant$35 GPa, respectively, combined with a high thermal stability [1–6], which is a little lower for the heterostructures [7–9] than for the nanocomposites [1]. The large increase of the hardness in the nanocomposites, as compared with TiN (20–21 GPa), was attributed to the TiN coating of 3–4 nm grain size, which prevents dislocation activity, and to 1 monolayer (ML) interfacial SiN_x [10], which is strengthened by valence charge transfer [11–15]. The SiN_x tissue connecting the grains enhances the strength of the nanocomposites by preventing grain boundary shear ('sliding'). The hardness enhancement in the heterostructures is commonly explained by the Koehler's model [15, 16].

The 1 ML thick SiN_x tissue in the TiN/SiN_x nanocomposites with randomly oriented TiN nanocrystals appears amorphous in x-ray diffraction (XRD) and electron diffraction [1, 13], whereas it is heteroepitaxially stabilized in the heterostructures [4]. The maximum hardness is achieved when the SiN_x layer is about 1 ML thick, but the hardness enhancement is lost when the thickness reaches 2 ML (see [1] and references therein) due to the weakening of neighbor Ti–N bonds [11]. The possibility of the formation of the epitaxial interfaces in TiN/SiN heterostructures was discussed in [4, 14–17]. Both the coherent and incoherent TiN/SiN_x interfaces were widely investigated in the frameworks of different first-principles procedures that were summarized in [18].

Whereas the large-scale industrial application for Ti–Al–Si–N and Cr–Al–Si–N nanocomposites as wear-protection coatings for tools was already found [19], the nanocomposite coatings based on Ti–Zr–N alloys were studied to a lesser extent. The authors showed that the Ti–Zr–N forms in a Ti–Zr–N/SiN_y nanocomposite coatings B1–$Ti_xZr_{1-x}N$ solid solution [3–5, 20] with a maximum nanohardness of about 40 GPa.

Because the investigation of the ternary nanocomposite M1–M2–N/SiN_x (where M1 and M2 are transition metals) is in its infancy, in this paper we investigate the $Ti_xZr_{1-x}N/SiN_y$ heterostructures as model systems using first-principles quantum molecular dynamics (QMD) calculations.

2. Experimental details and computational aspects

The coatings were obtained using vacuum-arc deposition from unit-cast Zr, Zr–Si, Ti–Zr and Zr–Ti–Si targets. The films were deposited in a nitrogen atmosphere. Deposition was carried out using standard vacuum-arc and high-frequency (HF) discharge methods. A bias potential was applied to the substrate from an HF generator, which produced impulses of convergent oscillations with $\leqslant$1 MHz frequency; every impulse duration was 60 μs, and the repetition frequency was about 10 kHz. Due to the HF diode effect, the value of the negative autobias potential occurring in the substrate was increased from 2 to 3 kV at the beginning of the impulse (after the start of the discharger operation). Coatings of 2.8–3.5 μm thickness were deposited onto steel substrates (of 20 and 30 mm diameter and 3–5 mm thickness). The deposition was performed without additional substrate heating. Zr–Ti–Si–N coatings were deposited on polycrystalline steel St.3 (C, 0.3 wt.%; the rest is Fe). The deposition temperature was 150–200 °C and the deposition rate was about 0.1 μm min^{-1}. Molecular nitrogen was employed as a reaction gas (table 1). There is a cathode current in A; P_N is the pressure of atomic nitrogen in Pa units; U_{HF} is the bias voltage of the HF discharge; and U is the bias voltage under conditions of vacuum-arc discharge.

Annealing was performed over 30 min in air using a furnace SNOL 8.2/1100 (Kharkiv, Ukraine) at temperatures of 300, 500 and 800 °C, and using the vacuum furnace SNVE-1.3, at a pressure of 5×10^{-4} Pa and temperatures of 300, 500 and 1180 °C. The heating and cooling rates were 10 and 30 °C min^{-1}, respectively [21]. It is known that Si_3N_4 is more stable than metal nitrides, which is consistent with their formation enthalpies: $\triangle H(Si_3N_4) = -745.1$ kJ mol^{-1}, $\triangle H(ZrN) = -365.5$ kJ mol^{-1}, $\triangle H(TiN) = -336$ kJ mol^{-1} [21, 22]. In addition, the crystallization temperature depends on the stoichiometry. For example, when α-$Si_3N_4/ZrN_x = 0.8$ ($x < 1$), the crystallization temperature determined from differential scanning calorimetry (DSC) curves is $T_{cr} = 1175$ °C; if α-$Si_3N_4/ZrN_x = 1.2$ ($x > 1$) then $T_{cr} = 1560$ °C [23, 24]. If the amorphous phase is over 50 vol.% in coating then the phase is thermally stable up to 1500 °C for super-stoichiometric ZrN_x ($x > 1$). Therefore, in this paper we chose an annealing temperature of 1180 °C, when ZrN crystallization occurs in accordance with work [25–27].

The morphology and surface topography of the coatings were studied using atomic force microscopy (NTEGRA Aura—NT-MDT) and the scanning electron microscope Quanta 200 3D.

Studies of phase compositions and structures were performed using the XRD device DRON-3M under filtered emission Cu-K_α, using the secondary beam of a graphite monochromator. Diffraction patterns were taken point-by-point with a scanning step 2Θ from 0.05° to 0.1°.

First-principles QMD calculations of the electronic structure were performed using the Quantum-ESPRESSO code [28] for the 8-atom cubic supercells of B1–$Ti_{4-n}Zr_nN_4$, $n = 0$, 1, 2, 3 and 4 random solid solution $Ti_{1-x}Zr_xN$, and for the 105-atomic hexagonal-like supercells of B1-$Ti_n Zr_{45-n}N_{45}(111)/Si_6N_9$, $n = 0$, 18, 27 and 45, representing the B1–$Ti_xZr_{1-x}N(111)/Si_3N_4$-like Si_2N_3 heterostructures. The heterostructures with 1 ML of Si_3N_4-like Si_2N_3 interfacial layer between 5 ML-thick B1–$Ti_xZr_{1-x}N(111)$, $x = 1.0$, 0.6, 0.4 and 0.0, slabs were investigated using first-principles QMD with the structure optimization as described in [28]. Several heterostructures with the partially segregated ('ordered') and random arrangement of the atoms within B1–$Ti_xZr_{1-x}N(111)$ slabs were considered. The 'ordered' structures were composed of the TiN and ZrN slabs. Figures 1 and 2 show the atomic configurations of the heterostructures under consideration. Vanderbilt ultra-soft pseudo-potentials were used to describe the electron–ion interaction [29]. In the Vanderbilt approach [30], the orbitals are allowed

Table 1. Samples and deposition conditions.

Evaporated materials	Coating	I_A (A)	P_N (Pa)	U_{HF} (V)	U_{bias} (V)	Note
Zr	ZrN	110	0.3	–	200	Standard technology
Zr	ZrN	110	0.3	200	–	HF deposition
Ti	TiN	90	0.3	200	200	HF deposition
Ti–Si	Ti_{40}–Si_{10}–N_{50}	100	0.3	200	–	HF deposition
Ti–Zr	Ti_{24}–Zr_{30}–N_{46}	95	0.3	200	–	HF deposition
Zr–Si	Zr_{35}–Si_{15}–N_{50}	110	0.3	200	–	HF deposition
Ti–Zr–Si	Ti_{45}–$Zr_{2.5}$–$Si_{7.5}$–N_{45}	100	0.3	200	–	HF deposition
Ti–Zr–Si	Ti_{30}–Zr_{20}–$Si_{7.5}$–$N_{43.5}$	100	0.3	200	–	HF deposition
Ti–Zr–Si	Ti_{20}–Zr_{35}–$Si_{7.5}$–$N_{37.5}$	100	0.3	200	–	HF deposition
Ti–Zr–Si	$(Ti_5$–Zr_{87}–$Si_8)N_{50}$	100	0.3	200	–	HF deposition

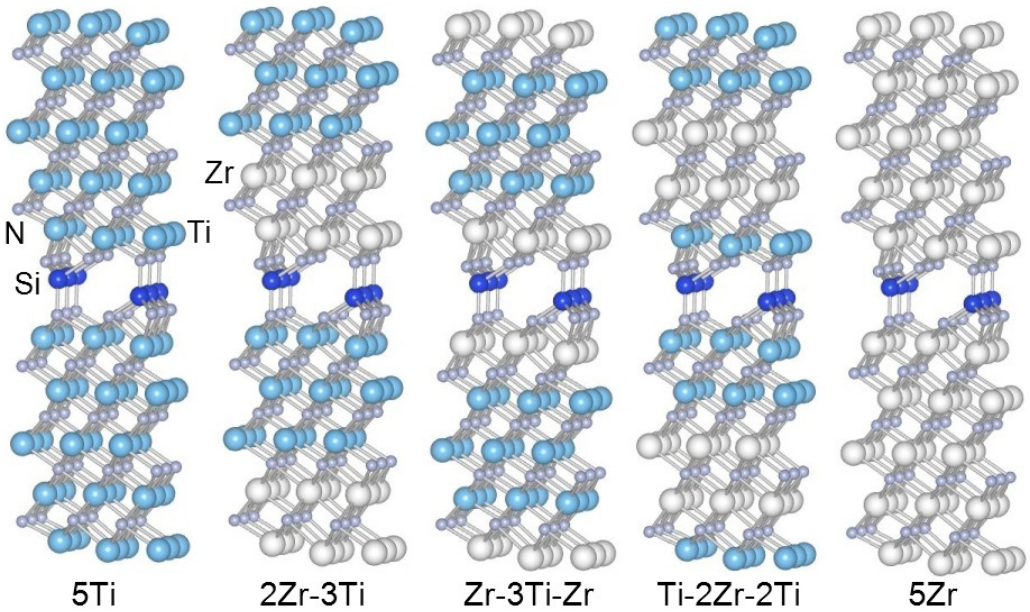

Figure 1. Atomic configurations of heterostructures consisting of TiN slabs ('5Ti' on the left), the partially segregated ('ordered') Ti-rich ($Ti_{27}Zr_{18}N_{45}/Si_6N_9$) slabs and ZrN slabs ('5Zr' on the right). The denotation of the heterostructures gives the sequence of layers in the *c*-direction. Here and in further figures, N are the small circles, Si are the dark circles, Ti are the dark large circles and Zr are the light large circles.

to be as soft as possible in the core regions so that their plane-wave expansion converges rapidly. The semi-core states were treated as valence states. For the titanium and zirconium pseudo-potentials, the nonlinear core-corrections were taken into account [28]. The generalized gradient approximation of Perdew *et al* [31] was employed to describe the exchange-correlation energy. The criterion of convergence for the total energy was 10^{-6} Ryd per formula unit. To speed up the convergence, each eigenvalue was convoluted with a Gaussian with a width of 0.02 Ryd. The cut-off energy for the plane-wave basis was set to 60 and 30 Ryd, for the 8- and 105-atomic unit supercells, respectively. The integration in the Brillouin zone (BZ) was done on special *k*-points determined according to the Monkhorst–Pack scheme [32] using a mesh (8 8 8) for the 8-atomic supercells and (2 2 2) for the 105-atomic supercells.

The QMD calculations of the initial relaxed heterostructures were carried out at 1130 °C with fixed unit cell parameters and volume (an NVT ensemble, i.e. a constant number of particles–volume–temperature) for ∼2.5 ps. In all of the QMD calculations, the time step was about 10^{-15} s. The temperature (1130–1180 °C) was chosen from the experimental results obtained by the DSC (beginning of ZrN-phase crystallization) at substoichiometric α-Si_3N_4/MeN_x (Me = metal, $x < 1$) [22, 26–29]. The system temperature was kept constant by rescaling the velocity. For the large-scale system calculations, only the Γ point was taken into account in the BZ integration. The variation of the total energy was considered during each QMD time step. During the initial 1–1.5 ps, all structures closely reached their equilibrium state and, at later times, the total energy of the equilibrated structures varied only slightly around the constant equilibrium value with the small amplitude of 0.025 eV atom^{-1}.

After QMD equilibration, the geometry of all heterostructures was optimized by simultaneously relaxing the atomic basis vectors and atomic positions inside the unit cells using the Broyden–Fletcher–Goldfarb–Shanno (BFGS) algorithm [33]. The relaxation of the atomic coordinates and the unit cell was considered to be complete when the atomic

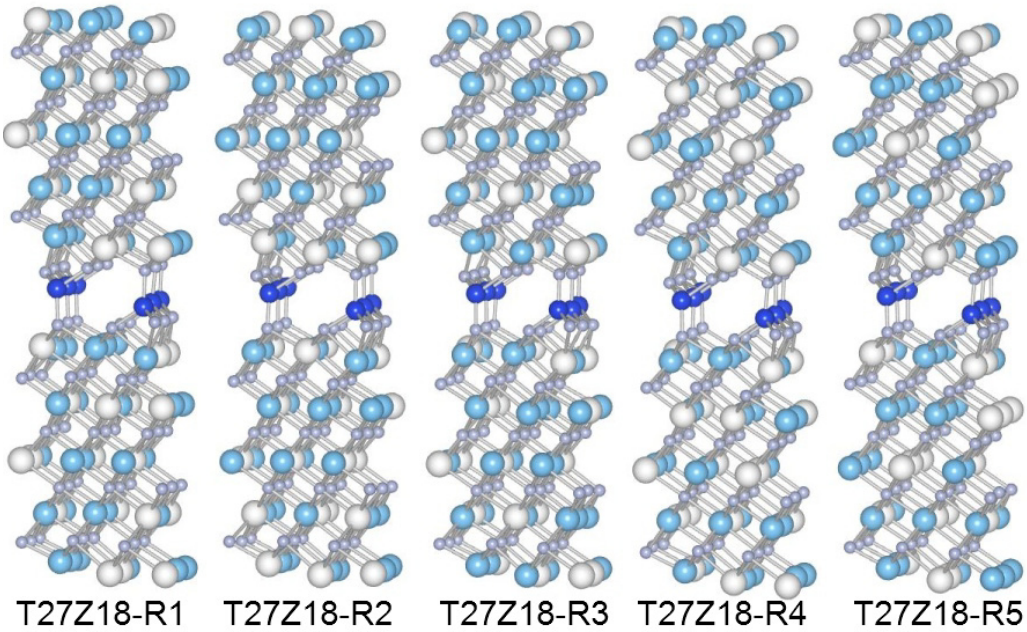

Figure 2. Atomic configurations of the Ti-rich random $Ti_{27}Zr_{18}N_{45}/Si_6N_9$ solution based heterostructures. The Zr-rich heterostructures are constructed from the corresponding Ti-rich heterostructures. In the denotation of the heterostructure, T and Z are Ti and Zr respectively, and the numbers are their concentrations.

forces were less than 1.0 mRyd au^{-1} (25.7 meV Å^{-1}), the stresses were smaller than 0.05 GPa, and the total energy varied by less than 0.1 mRyd (1.36 meV) during the iterative structural optimization process.

The formation energy of the $Ti_{1-x}Zr_xN$ solid solution (E_{form}) and of the heterostructures (E_{hetero}) was determined from equations (1) and (2), respectively, as a function of composition x:

$$E_{form}(x) = E_T(Ti_{1-x}Zr_xN) - (1-x)E_T(TiN) - xE_T(ZrN), \quad (1)$$

$$E_{hetero}(x) = E_T(Ti_{1-x}Zr_xN/SiN_y) - (1-x)E_T(TiN/SiN_y) - xE_T(ZrN/SiN_y), \quad (2)$$

E_T is the total energy of $Ti_{1-x}Zr_xN$ solid solutions, stoichiometric TiN and ZrN compounds, and $Ti_{1-x}Zr_xN/SiN_y$, TiN/SiN_y and ZrN/SiN_y heterostructures.

3. Results and discussion

3.1. Computation results and discussion

Figure 3 shows the dependence of the lattice parameter a on the concentration of TiN and ZrN for the $Ti_{1-x}Zr_xN$ solid solution.

The calculated values are slightly higher than the experimental ones by approximately 0.2–0.5%, and display a slight positive deviation from the mixing rule $a(x) = xa\mathrm{ZrC} + (1-x)a\mathrm{TiC}$, in agreement with the experiment [5].

The Gibbs free energy of mixing of $Ti_{1-x}Zr_xN$, calculated at zero temperature (i.e. formation energy), as a function of composition x, is shown in figure 4. The formation

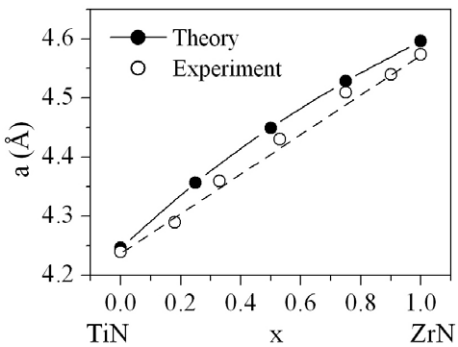

Figure 3. Demonstration of $Ti_{1-x}Zr_xN$ lattice parameters versus composition. The experimental data were taken from our research. The dashed line reflects the mixing rule for the experimental results. Here and in the following figures, the solid line is a polynomial fit to the data points.

energy is positive in the entire composition range, which implies that the alloys are metastable, and should decompose into TiN and ZrN with the chemical driving force E_{Form}, in agreement with the theoretical results in [5]. Because the mixing entropy term stabilizes the solid solution, and this stabilization increases with increasing temperature, the positive value of the Gibbs free energy in figure 4 is due to the mixing enthalpy term.

We performed the QMD optimization of the structure of the initial epitaxial heterostructures at zero temperature and at 1130 °C with subsequent variable-cell structural relaxation. The arrangement for all interfaces was found to be preserved, as shown in figures 1 and 2. The structural parameters and the total energies of the computed heterostructures are summarized in tables 2–4. One can see from tables 3 and 4 that, for the same concentration x, the structural parameters

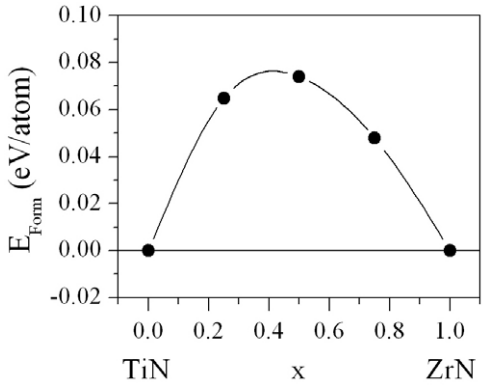

Figure 4. Computed formation energy (E_{Form}) for $Ti_{1-x}Zr_xN$ as a function of the composition x.

Table 2. Structural parameters and total energy of the $Ti_{45}N_{45}/Si_6N_9$ (5Ti) and $Zr_{45}N_{45}/Si_6N_9$ (5Zr) heterostructures (see figure 1).

	A (Å)	B (Å)	c (Å)	V (Å^3 atom^{-1})	E_T (eV atom^{-1})
5Ti	8.974	8.915	14.863	9.826	−828.325
5Zr	9.730	9.607	15.865	12.263	−726.329

Table 3. Structural parameters and total energy of the $Ti_{27}Zr_{18}N_{45}/Si_6N_9$ (i.e. $Ti_{0.6}Zr_{0.4}N/Si_2N_3$) heterostructures (see figures 1 and 2) ($0.6 \times E_T(Ti_{45}N_{45}/Si_6N_9) + 0.4 \times E_T(Zr_{45}N_{45}/Si_6N_9) = -787.52\,659$ eV atom^{-1}).

Heterostructure	a (Å)	b (Å)	c (Å)	V (Å^3 atom^{-1})	E_T (eV atom^{-1})
2Zr–3Ti	9.292	9.202	15.291	10.813	−787.484
Zr–3Ti–Zr	9.278	9.192	15.337	10.814	−787.485
Ti–2Zr–2Ti	9.319	9.217	15.238	10.824	−787.485
Average	9.297	9.203	15.289	10.817	−787.485
T27Z18–R1	9.311	9.215	15.316	10.873	−787.488
T27Z18–R2	9.315	9.214	15.300	10.856	−787.489
T27Z18–R3	9.313	9.218	15.325	10.885	−787.484
T27Z18–R4	9.318	9.202	15.355	10.904	−787.475
T27Z18–R5	9.314	9.212	15.345	10.887	−787.475
Average	9.314	9.212	15.328	10.881	−787.482

weakly depend on the atomic arrangements. The average cell volume for the disordered structures is higher than that of the ordered one.

The total energy calculations show that the Ti–Zr–N solid solution, which forms during the deposition, is metastable and should decompose into stoichimetric TiN and ZrN. However, by analogy with other similar systems, such as Ti–Al–N and Cr–AlN, this decomposition is activated and therefore it will occur only at somewhat higher temperature. (Of course, the mixing entropy term will stabilize the random solid solution at high temperatures approaching the melting point, where the destabilizing mixing entropy term will diminish.)

However, in $Ti_{1-x}Zr_xN/SiN_x$ heterostructures, the different stability of heterostructures, composed of ordered and random $Ti_{1-x}Zr_xN$ solid solution slabs which terminated with Zr or Ti atoms at the SiN_x interface, indicates that the decomposition of the random solid solution can be accelerated at lower temperature. Finally, we would like to emphasize that our estimation of the $Ti_{1-x}Zr_xN$ solid solution

Table 4. Structural parameters and total energy of the $Ti_{18}Zr_{27}N_{45}/Si_6N_9$ (i.e. $Ti_{0.4}Zr_{0.6}N/Si_2N_3$) heterostructures (see figures 1 and 2) ($0.4 \times E_T(TiN/Si_2N_3) + 0.6 \times E_T(ZrN/Si_2N_3) = -767.12\,736$ eV atom^{-1}).

Heterostructure	a (Å)	b (Å)	c (Å)	V (Å^3 atom^{-1})	E_T (eV atom^{-1})
2Ti–3Zr	9.451	9.345	15.491	11.316	−767.087
Ti–3Zr–Ti	9.463	9.355	15.439	11.306	−767.089
Zr–2Ti–2Zr	9.425	9.324	15.568	11.309	−767.085
Average	9.446	9.341	15.499	11.310	−767.087
T18Z27–R1	9.464	9.356	15.505	11.365	−767.088
T18Z27–R2	9.472	9.343	15.520	11.355	−767.086
T18Z27–R3	9.463	9.352	15.512	11.359	−767.093
T18Z27–R4	9.466	9.367	15.487	11.363	−767.098
T18Z27–R5	9.465	9.363	15.497	11.353	−767.098
Average	9.466	9.356	15.504	11.359	−767.093

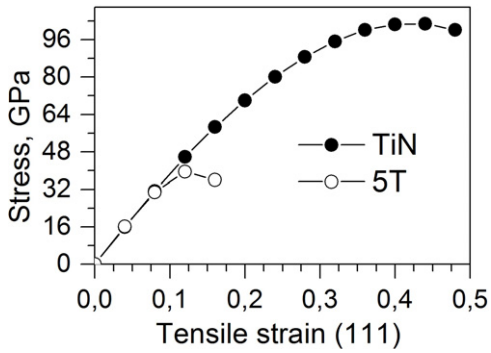

Figure 5. Calculated stress–strain curves for tension in the (111) direction for the bulk TiN (full circles) and 5Ti ($TiN(111)/Si_2N_3$ heterostructure) (open circles).

stability is based on the comparison of the total energies of different heterostructures. Vibrational and configuration entropies should be taken into account for a more detailed analysis.

Below, we show that the nanocomposite Ti–Zr–Si–N coatings exhibit improved mechanical properties compared to those of the nanocomposite coatings based on pure Ti–Zr–N alloys. To understand this phenomenon at the atomic level, we should calculate the stress–shear strain curves for our generated heterostructures. However, these large-scale calculations demand much computational time due to the bed convergence of shear stress. There is another way to clarify the possible origin of the strength enhancement of the nanocomposites based on SiN_x. We calculated the stress–tensile strain relations for pure TiN and the 5Ti ($TiN(111)/Si_2N_3$) heterostructure using the BFGS procedure for the optimization of both the unit cell vectors and atomic coordinates within the unit cell. The stress–tensile strain curves for TiN and T5 structures are shown in figure 5.

One can see from figure 5 that the formation of the Si_3N_4 interface in TiN(111) leads to a reduction of ideal tensile strength. The interface formation does not result in strengthening the nanocomposites from a chemical bonding perspective. It follows that the formation of the interfacial Si_3N_4-like layer in TiN(111) strongly destabilizes titanium nitride. Based on these results, we can suppose that the observed strength enhancement in the transition

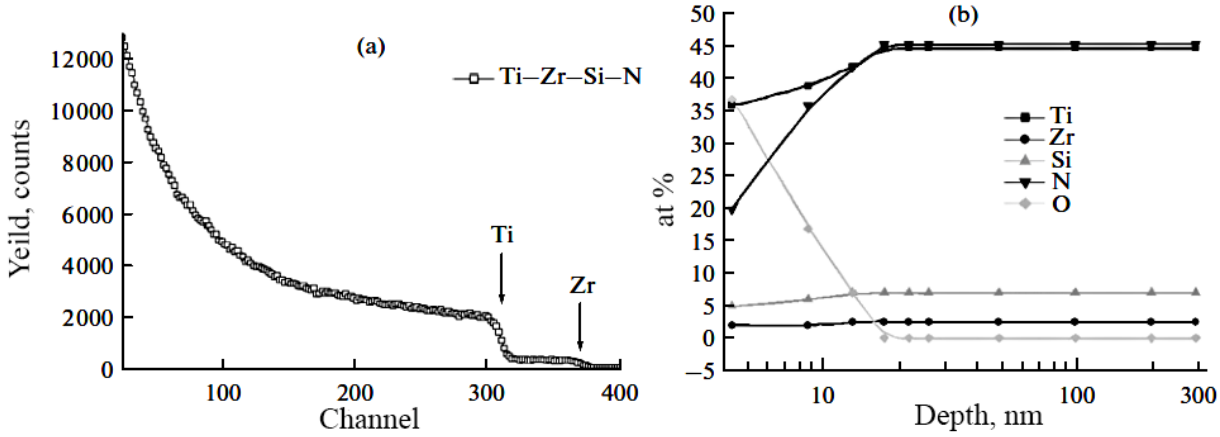

Figure 6. Results of the Ti–Zr–Si–N specimen analysis: (a) spectra of rotating reflection; (b) modeling results of the elements' concentration of the multilayered Ti–Zr–Si–N specimen.

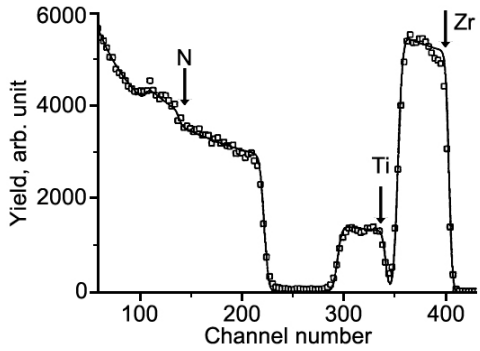

Figure 7. Energy spectrum of the 1.35 MeV He^+ ion measured for a Ti, 24%, Zr, 30%, N, 46% nanocomposite coating; arrows indicate kinematical boundaries of elements on the substrate single crystal Si.

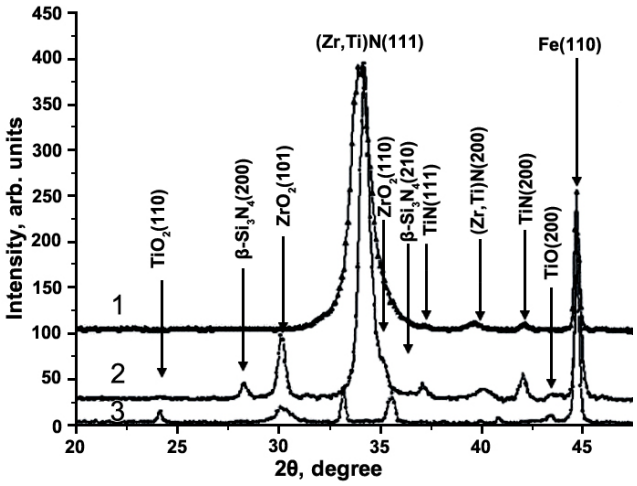

Figure 8. Part of the XRD patterns taken for the condensates of the Zr–Ti–Si–N system after deposition (1); after 30 min' annealing in a vacuum, under $T_{an} = 1180\,^{\circ}C$ (2) and under $T_{an} = 800\,^{\circ}C$ in air (3). Three peaks, which are not designated in the curve, are for an oxide (Fe_2O_3) of the Fe substrate (JCPDS 33-0664).

metal nitride–Si_3N_4-based nanocomposite coatings should be ascribed mostly to the interfaces that play the role of barriers inhibiting dislocation motion.

3.2. Experimental results and disscussion

Figure 6(a) presents the Rutherford backscattering (RBS) results obtained from the Ti–Zr–Si–N coatings, deposited on steel specimens. It is quite evident that the He ion beam energy is insufficient to analyze the film thickness. But Ti and Zr peaks are very well separated, and it is apparent that Ti and Zr concentrations are distributed almost uniformly throughout the coating depth. Figure 6(b) shows the simulation results of the elements' concentration through the layers in the Ti–Zr–Si–N coatings. This figure shows clearly that Ti and N concentrations differ strongly on the surface and just beneath it due to the residual atmosphere in the source chamber. But from a depth of 10 nm, their concentrations become equal ∼45 at.%, while the Si concentration is about 7 at.% and the Zr concentration is only 3 at.%.

Figure 7 shows that at concentrations of Ti = 24 at.%, Zr = 30 at.% and N of about 46 at.%, obtained by RBS analysis (using a simulation of the correlation of the elements' concentrations), we observed retention thermal stability of the material up to a temperature of 1200 °C (see figure 8) [33].

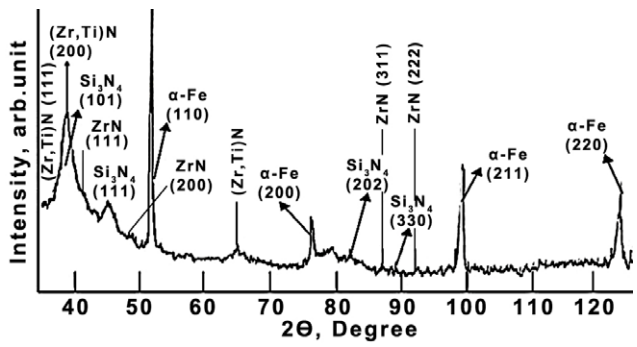

Figure 9. XRD pattern taken for the coatings of the Ti_{30}–Zr_{20}–$Si_{7.5}$–$N_{43.5}$ system after deposition (the thickness is 2.8 μm).

The increase of concentration of Ti and Si elements leads to the formation of three phases: solid solution nc-(Zr, Ti)N, ZrN-nc and α-Si_3N_4, as is seen from figure 9 where difractogram of the Zr–Ti–Si–N coatings is shown.

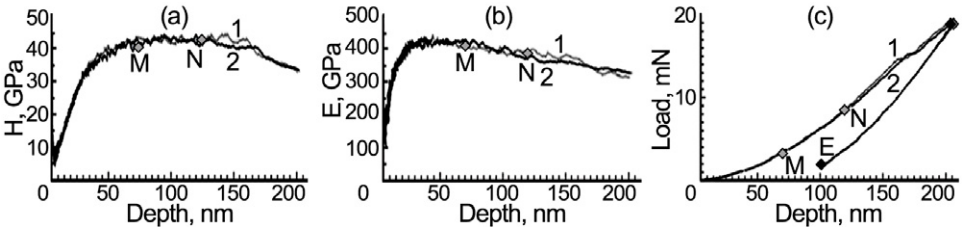

Figure 10. The dependences of hardness (a), elastic modulus (b) on the indentation depth and dependence of indentation depth on the applied load (c). M and N are control points; E is an endpoint of unloading; 1 and 2 are experiment numbers.

Table 5. The hardness and elastic modulus of nanocomposite coatings (Zr_{70}–Ti_{22}–Si_8)N before and after annealing.

Mechanical characteristics	After deposition	$T_{an} = 300\,^{\circ}C$ vacuum	$T_{an} = 500\,^{\circ}C$ vacuum	$T_{an} = 300\,^{\circ}C$ air	$T_{an} = 500\,^{\circ}C$ air
H (GPa)	40.8	43.7	48.6	38.7	55
E (GPa)	382	424	456	373	400
H/*E*	0.11	0.1	0.108	0.1	0.135

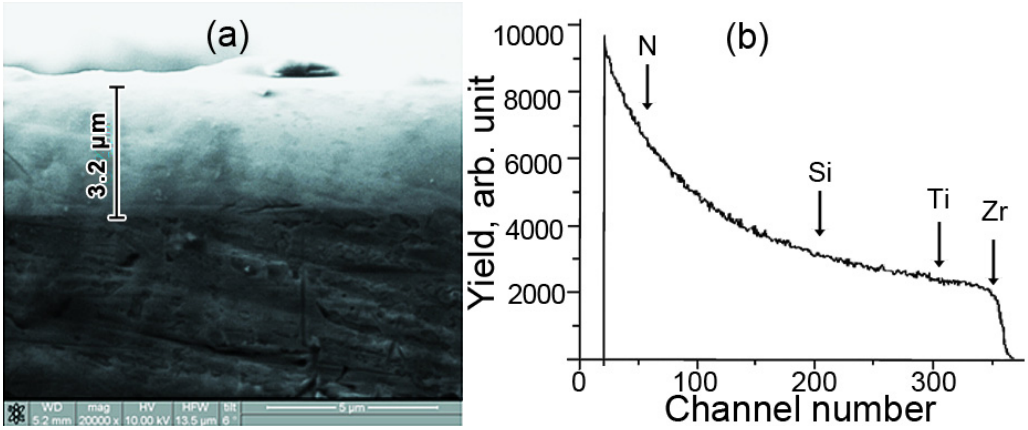

Figure 11. Cross-sectional SEM image (WD = 5.2 mm, mag: 20 000×, HV = 10 kV) of hard coating Ti_{20}–Zr_{35}–$Si_{7.5}$–$N_{37.5}$ (Si, N—high concentration) (a) and energy spectrum for Zr–Ti–Si–N nanocomposite coating, measured by RBS with 1.35 MeV $4He^{+}$ ions' energy (b). Arrows indicate the kinematical boundaries of the elements.

It was observed that the maximum hardness ≈40 GPa (see figure 10), which was increased after annealing in air medium at 500 °C to 55 GPa and was increased to 48 GPa after annealing in a vacuum (see table 5). That is, very high values of hardness up to 55 GPa can be obtained (as a result of the finished process of spinodal segregation; orientation amorphous phases at nanograin boundaries of the solid solution (Zr,Ti)N and ZrN with sizes 10–12 and 4–6.5 nm correspondingly) when the heterostructure (nanocomposite) is formed. After annealing at 1180 °C, the grain size of the solid solution increased to 25 nm and the concentration of packing defects increased almost to 15%. Also, we received a small peak (XPS analysis, which will be discussed later) that points to the formation of a small amount of Si–O at 103.9 eV (after annealing in a vacuum at a temperature of 1180 °C for 30 min).

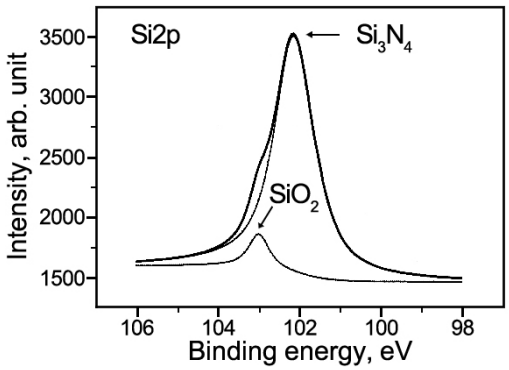

Figure 12. XPS analysis results of hard coating Ti_{20}–Zr_{35}–$Si_{7.5}$–$N_{37.5}$.

Figure 11(a) shows the film cross-section, which demonstrates that in the course of deposition no cracks were found, which indicates the good quality of the coating. The energy spectrum of ion backscattering measured for Zr–Ti–Si–N samples on the steel substrate is shown in figure 11(b). Since Zr and Ti concentrations were high, this spectrum could hardly help to determine Si and N background concentrations. Measurements of Si and N concentrations using the RBS spectra gave a higher error than for Zr and Ti. But the Si concentration was not less than 7 at.%, while the nitrogen concentration might reach more than 40 at.% (43%) when the rounding is ±3% (in nitrogen concentration).

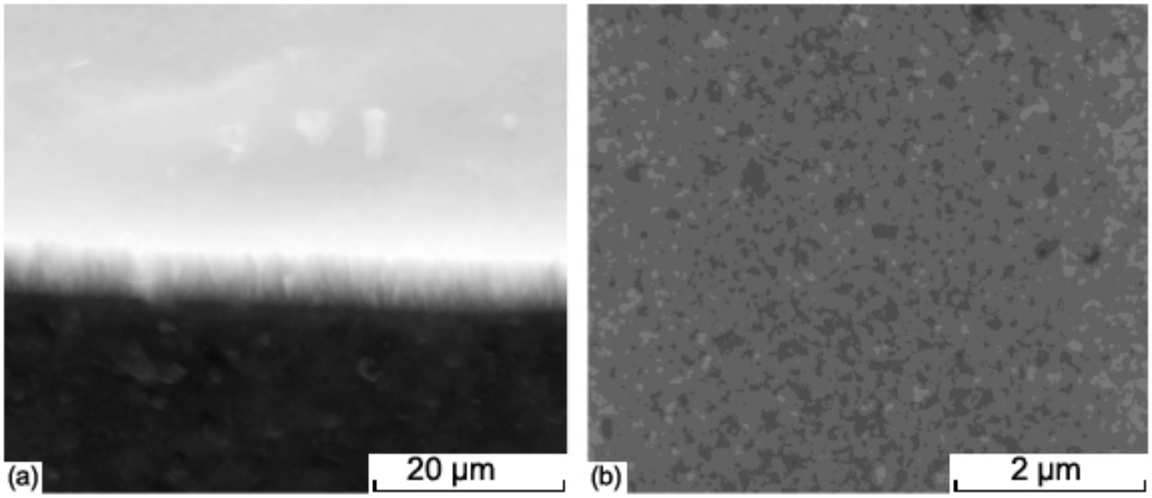

Figure 13. SEM images of $(Ti_5–Zr_{87}–Si_8)N_{50}$ coatings with columnar structure: coating cross-section (a), and coating surface topography (b).

For these series of samples (with Si $\geqslant$ 5.8 at.%), we provided an investigation of Si–N_x compounds using XPS analysis. It showed a high peak on the 101.9 eV level which points directly to the formation of Si–N_x compounds.

The coatings' deposition was carried out at a temperature about 200 °C, but it needed 500–800 °C to complete segregation according to theoretical and practical works. At these temperatures, the process of building $SiN_x(\alpha\text{-}Si_3N_4)$ can be completed [26]. The evidence of this is the direct experimental results of XPS-analysis in figure 12. They indicate the formation of SiN_x bonds after annealing at 800 °C. Also, we see a small peak corresponding to the formation of a SiO_x phase. RBS and scanning electron microscopy (SEM) analysis indicate the formation (growth) of the coating thickness to 2.8 μm (the accuracy of thickness determination is about 1 nm).

Morphology and structure research of the cross-sections of specimens with obtained Ti–Si–N and Ti–Zr–Si–N coatings evidences a clear-cut columnar structure (figure 13), with columns' diameter 10–25 nm and 0.1 μm.

Each grain of 0.1 μm size contains a multitude of subgrains. For this reason, the crystallites are actually smaller than the width of the columnar grains and their grain size is about 60 nm.

These results indicate that the amount of N was essentially high, which allowed it to form nitrides with Zr, Ti or (Zr, Ti)N solid solution. Concentration of Si was low (about 7–8 at.%), but it was enough to form siliconitride phases.

The three-dimensional islands on the films' surface with the columnar structure are the spots where the end faces of individual grains appear on the surface (see figure 13). The listed mean quadratic roughness of the film surface (R_{rms}) is obtained with atomic force microscopy. It is evident that the roughness depends both on the chemical composition and the parameters of deposition. The waviness of the coatings is due to the mechanism of growth, i.e. the formation of individual islands on the surface (the Folmer–Weber mechanism). The condition of its implementation is the predominance of the interaction between adjacent atoms compared to the interaction of these atoms and the substrate. The small nuclei in the island formation mode appear straight on the substrate surface and then grow, turning into larger islands of the condensed phase and giving rise to intergrain recesses due to the masking effect, and resulting in a granular structure. Figure 14 shows the surface topography of the Ti–Zr–Si–N coatings.

The XRD measurements revealed that the Ti–Zr–Si–N coating has a uniphase crystalline structure of the solid solution (Zr, Ti)N [34]. Silicon nitride is not observed as a separate phase, apparently due to the significant reduction of silicon in the coating under the arc plasma effect. This occurs because the volume fraction is less than the detection limit of XRD analysis and the Si concentration is not enough to form a ML around (Zr, Ti)N or ZrN (TiN). The structure of the Ti–Si–N and Ti–Zr–Si–N coatings is characterized by a higher level of lattice microdeformations (over 1%) [35]. The larger lattice microdeformations prove that the composition has chemical inhomogeneity in each coating phase. The coatings have a vividly pronounced texture. The condensation compressive stresses in the film of the solid solution (Zr, Ti)N causes textures' formation [36]. The approximate crystallite sizes of (Zr, Ti)N solid solution is $L = 25$ nm. Information about the hardness H, elastic modulus E, effective Young's modulus $E^* = E/(1-\nu^2)$, H/E^* ratio and H^3/E^{*2} ratio for the obtained coatings is shown in table 6 [24, 25, 37].

The x-ray structural analytical method (figure 8) was employed to examine the friction paths left by high temperature tests. The surface of the friction paths shows ZrO_2 (8.5 vol.%) and TiO_2 (12.5 vol.%) oxides and TiN (20 vol.%), β-Si_3N_4 (6.5 vol.%) and (ZrTi)N (52.5 vol.%) nitrides. Unlike in the case of friction at room temperature, the high temperature intensifies oxidation, followed by the reduction of the destroyed oxide films.

Changed diffraction lines were related to increased crystalline sizes (in general) and decreased micro-deformation. The formation of three phases in coating

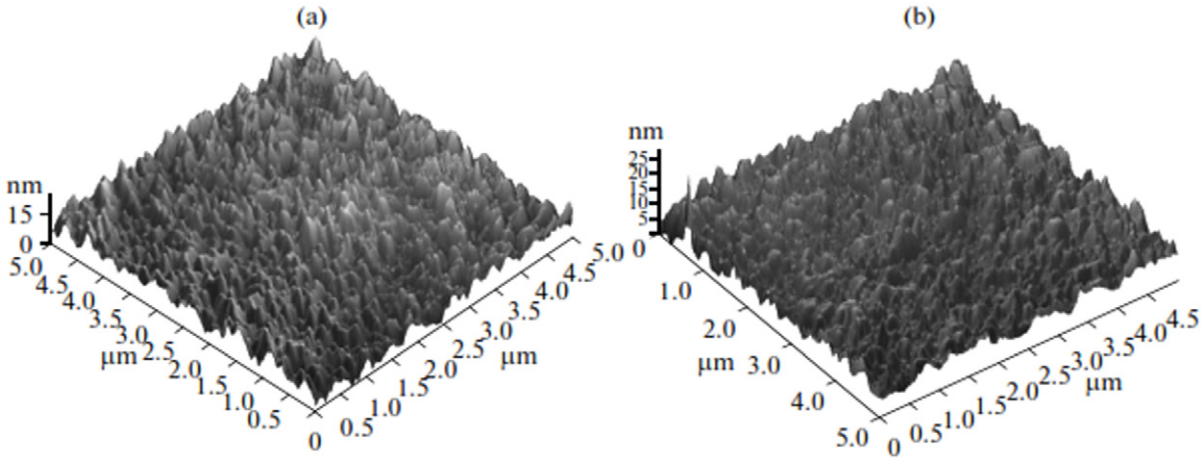

Figure 14. Surface topography of Ti–Zr–Si–N coating: (a) Ti = 22.73 at.%, Zr = 2.12 at.%, Si = 3.05 at.% (R_{rms} = 3.359 94 nm); (b) Ti = 27.46 at.%, Zr = 2.51 at.%, Si = 3.76 at.% (R_{rms} = 2.289 27 nm).

Table 6. Some physical and mechanical properties of the obtained coatings.

	H (GPa)	E (GPa)	E^* (GPa)	H/E^*	H^3/E^{*2} (GPa)
TiN	28	312	338.54	0.08	0.19
Ti–Si–N	38–39	356	386.28	0.10	0.40
Ti–Zr–Si–N	38–41	478	518.66	0.08	0.26

Ti–Zr–Si–N with volume fractions of (Zr, Ti)N-nc—57 vol.%, ZrN-nc—35 vol.% and α-$Si_3N_4 \geqslant 7.5$ vol.%, as well as the formation of small sized nanograins of 4–6 nm in (Zr, Ti, N) and 10–12 nm in ZrN, leads to increasing nanohardness up to 48–55 GPa—superhardness. Annealing in a vacuum below 500 °C finished the process of spinodal segregation at grain boundaries and interfaces. Annealing stimulated segregation processes and formed a stable modulated coating structure. XRD patterns were taken for the coatings of the Zr–Ti–Si–N system after deposition (figure 9). The relative intensities of the peaks indicate amorphous β-Si_3N_4, α-Fe phase crystallites and a metallic sublattice of (Zr, Ti)N solid solution.

Figure 15 shows an XRD pattern of volume phases for a nanostructured Zr–Si–N coating with 10–12 nm grain sizes for the nc-Zr_xN phase (where nc is a nanocrystalline phase) which are coated by a ML of the α-Si_3N_4 (amorphous phase).

Analyzing the phase composition of Zr–Ti–Si–N films, we found that a basic crystalline component of the as-deposition state was solid solution (Zr, Ti)N based on a NaCl-type cubic lattice. Table 7 presents XRD data: a lattice period in non-stressed cross-section (a_0), value of macrodeformation ε, microdeformation $\langle\varepsilon\rangle$ and concentration of packing defects $\alpha_{\text{def.pack}}$. The data were obtained both for samples after coating deposition and for those annealed in vacuum and air at various temperatures. Crystallites of the solid (Zr, Ti)N solution underwent compressing elastic macrostresses occurring in a 'film–substrate' system. Compressing stresses, which were present in a plane of growing film, indicated the development of compressing

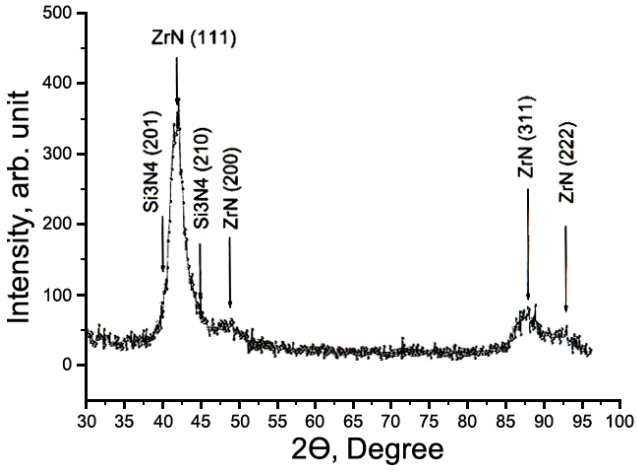

Figure 15. A fragment of the diffraction pattern for the Zr_{35}–Si_{15}–N_{50} coating deposited by the vacuum-arc method with HF stimulation (Fe–K radiation).

deformation in a crystal lattice, which was identified by a shift of diffraction lines in the process of angular surveys ('$\sin^2\psi$ method') and reached a 2.93% value (table 7). With an $E \approx 400$ GPa characteristic elastic modulus and 0.28 Poisson coefficient, the deformation value corresponded to that occurring under the action of compressing stresses $\sigma_c \approx -8.5$ GPa. We should also note that such high stresses characterize nitride films, which were formed under deposition with a high radiation factor. This provides a high adhesion to the base material and the development of compression stresses in the film, which was stiffly bound to the base material due to an 'atomic peening' effect.

Figures 10(a) and (c) present the results of hardness and elastic modulus measurements for the Zr–Ti–Si–N coating using a trihedral Berkovich pyramid. The points at these dependences indicate places where the values of H and E were estimated. Curves 1 and 2 correspond to the different measurements of the same sample. As seen from these dependences, $H = 42.7$ GPa and $E = 390 \pm 17$ GPa for this

Table 7. Changes of structure and substructure parameters occurring in ion-plasma deposited films of a Zr_{35}–Ti_{20}–$Si_{7.5}$–$N_{37.5}$ system in the course of high-temperature annealing in vacuum and in air.

Parameters of structure	After deposition	$T_{an} = 300\,^{\circ}C$ vacuum	$T_{an} = 500\,^{\circ}C$ vacuum	$T_{an} = 1100\,^{\circ}C$ vacuum	$T_{an} = 300\,^{\circ}C$ air	$T_{an} = 500\,^{\circ}C$ air
a_0 (nm)	0.455 20	0.452 26	0.451 49	0.450 64	0.453 15	0.451 95
ε (%)	−2.93	−2.40	−1.82	−1.09	−2.15	−1.55
$\langle\varepsilon\rangle$ (%)	1.4	1.0	0.85	0.8	0.95	0.88
$\alpha_{def.pack}$	0.057	0.085	0.107	0.150	0.090	0.128

type of coating. Figure 10(c) shows the dependence of indentation depth on the applied load to the indenter.

When the radius of the bluntness of the Berkovich pyramid is above 20 μm, the actual values of hardness and elastic modulus can be obtained at a depth from 70 to 150 nm (which is noticeably less than 1/10 of the coating thickness 2.8 μm) [38–41]. Points at which the measurements were made are labeled N and M. To obtain reliable information (without an oxide layer which was about 15–17 nm at as-deposited coating), the hardness measurement was carried out by an oblique microsection at an angle 7°.

4. Conclusions

We performed first-principles investigations of the B1–$Ti_xZr_{1-x}N(111)/Si_3N_4$-like Si_2N_3 heterostructures for $x = 1.0$, 0.6, 0.4 and 0.0, and of the B1–$Ti_xZr_{1-x}N$ solid solutions for $x = 1.0$, 0.75, 0.5, 0.25 and 0.0. Several heterostructures with the segregated ('ordered') and random arrangement of the atoms within B1–$Ti_xZr_{1-x}N(111)$ slabs were considered. The ordered structures consisted of TiN and ZrN layers. The ordered heterostructures, in which the Zr atoms surround the SiN_x interface, were found to be the most stable. According to our results, the $B1 - Ti_xZr_{1-x}N(111)/Si_3N_4$-like Si_2N_3 nanostructures should decompose into the $TiN(111)/SiN_y$ and $ZrN(111)/SiN_y$ units due to the immiscibility of TiN and ZrN. However, our experiment shows that during the deposition at relatively low temperature, B1–$Ti_xZr_{1-x}N$ metastable solid solutions can form. According to our results, the formation of the random B1–$Ti_xZr_{1-x}N$ solid solution will be preferable for the Zr-rich heterostructures, whereas for the Ti-rich heterostructure, ordered alloys should form.

The Zr–Ti–Si–N-based superhard nanostructured coatings of different chemical compositions were deposited under different growth conditions. An analysis of the coatings' properties and structure was carried out. Nanostructured and nanocomposite materials based on Ti–Zr–Si–N, Ti–Zr–N, Ti–Si–N and Ti–N, with concentrations of 5–45 at.% Ti, 2.5–87 at.% Zr and a similar concentration of Si (6–10 at.%), were analyzed. Thus almost all coatings consisted of stoichiometric nitrides, except one series in which the covers were superstoichiometric nitrides ZrN_x ($x > 1$).

It was determined that the size of the nanograins of the solid solution changed from 10 to 12 nm. At the same time, the size of the α-Si_3N_4 interlayer, which enveloped the (Ti, Zr)N nanograins, ranged from 6 to 8 nm.

The mechanical properties (hardness and elastic modulus) varied depending on the annealing temperature.

Acknowledgments

This work has been done under financial support of the Ministry of Education and Science of Ukraine within the government program order no. 411 and in collaboration with National Institute of Materials Science, Tsukuba, Japan; partially within research projects 0112U001382 'Designing of the basis of formation of multicomponent nanostructured superhard coatings with high physical and mechanical properties' and 'Physical principles of plasma technologies for complex processing of multicomponent materials and coatings' (number 0113U000137c). We are grateful to Professor O V Sobol, V M Beresnev (Kharkiv) and V V Uglov (Minsk) for help with the experiments. Parts of this work were presented as an oral report at the International Conference 'Nanomaterials: Applications and Properties '2012', 17–22 of September 2012, Alushta, the Crimea, Ukraine.

References

[1] Beresnev V M, Kaverin M V, Akhmed M M, Smolyakova M Yu, Kolesnikov D A, Kirik G V, Komarov F F, Grudnitskii V V and Nemchenko U S 2012 *J. Friction Wear* **33** 167–73

[2] Pogrebnjak A D, Beresnev V M, Demianenko A A, Baidak V S, Komarov F F, Kaverin M V, Makhmudov N A and Kolesnikov D A 2012 *Phys. Solid State* **54** 1882–90

[3] Sobol' O V, Pogrebnyak A D and Beresnev V M 2011 *Phys. Met. Metallogr.* **112** 188–95

[4] Pogrebnjak A D *et al* 2012 *J. Nanosci. Nanotechnol.* **12** 9213–19

[5] Pogrebnjak A D *et al* 2010 *Nanostruct. Mater. Nanotechnol. IV: Ceram. Eng. Sci. Proc.* **31** 127–38

[6] Pogrebnyak A D, Shpak A V, Azarenkov N A and Beresnev V M 2009 *Phys.-Usp.* **52** 29–54

[7] Pogrebnjak A D and Beresnev V M 2012 Hard nanocomposite coatings, their structure and properties *Nanocomposites—New Trends and Developments* ed F Ebrahimi (Croatia: InTech) pp 123–60

[8] Veprek S, Veprek-Heijman M G J, Karvankova P and Prochazka J 2005 *Thin Solid Films* **476** 1–29

[9] Veprek S, Zhang R F, Veprek-Heijman M G J, Sheng S H and Argon A S 2010 *Surf. Coat. Technol.* **204** 1898–906

[10] Chen Y H, Lee K W, Chiou W A, Chung Y W and Keer L M 2001 *Surf. Coat. Technol.* **146–147** 209–14

[11] Söderberg H, Odén M, Molina-Aldareguia J M and Hultman L 2005 *J. Appl. Phys.* **97** 114327–8

[12] Hoerling A, Sjölén J, Willman H, Larson T, Odén M and Hultman L 2008 *Thin Solid Films* **516** 6421–31

[13] An T, Wen M, Wang L L, Hu C Q, Tian H W and Zheng W T 2009 *J. Alloys Compd.* **486** 515–20
[14] Veprek S, Argon A S and Zhang R F 2007 *Phil. Mag. Lett.* **87** 955–66
[15] Zhang R F, Argon A S and Veprek S 2009 *Phys. Rev. Lett.* **102** 015503
Zhang R F, Argon A S and Veprek S 2009 *Phys. Rev.* B **79** 245426
Zhang R F, Argon A S and Veprek S 2010 *Phys. Rev.* B **81** 245418
[16] Koehler J S 1970 *Phys. Rev.* B **2** 547–52
[17] Veprek S and Reiprich S 1995 *Thin Solid Films* **268** 64–71
[18] Hultman L, Barenõ J, Flink A, Söderberg H, Larsson K, Petrova V, Odén M, Greene J E and Petrov I 2007 *Phys. Rev.* B **75** 155437
[19] Söderberg H, Odén M, Larsson T, Hultman L and Molina-Aldareguia J M 2006 *Appl. Phys. Lett.* **88** 91902–3
[20] Söderberg H, Odén M, Flink A, Brich J, Persson P O A, Beckers M and Hultman L 2007 *J. Mater. Res.* **22** 3255–64
[21] Musil J and Zeman P 2007 *Solid State Phenom.* **127** 31–6
[22] Musil J 2012 *Surf. Coat. Technol.* **207** 50–65
[23] Musil J 2000 *Surf. Coat. Technol.* **125** 322–30
[24] Musil J 2006 *Nanostructured Coatings* ed A Cavaleiro and J Th M de Hosson (New York: Springer) chapter 10, pp 407–63
[25] Musil J, Baroch P and Zeman P 2008 *Plasma Surface Engineering Research and its Practical Applications* ed R Wei (Kerala: Research Signpost) pp 1–34
[26] Fallqvist A, Ghafoor N, Fager H, Hultman L and Persson P O Å 2013 *J. Appl. Phys.* **114** 224302
[27] Musil J, Vlček J and Zeman P 2008 *Adv. Appl. Ceram.* **107** 148–54
[28] Baroni S *et al* www.pwscf.org
[29] Vanderbilt D 1990 *Phys. Rev.* B **41** 7892–5
[30] Hu X, Zhang H, Dai J, Li G and Gu M 2005 *J. Vac. Sci. Technol.* A **23** 114–8
[31] Perdew J P, Burke K and Ernzerhof M 1996 *Phys. Rev. Lett.* **77** 3865–8
[32] Monkhorst H J and Pack J D 1976 *Phys. Rev.* B **13** 5188–92
[33] Billeter S R, Curioni A and Andreoni W 2003 *Comput. Mater. Sci.* **27** 437–45
[34] Ivashchenko V I, Veprek S, Turchi P E A and Shevchenko V I 2012 *Phys. Rev.* B **85** 195403–15
[35] Veprek S and Veprek-Heijman M G J 2008 *Surf. Coat. Technol.* **202** 5063–73
[36] Pogrebnjak A D and Vyacheslav M B 2012 *Nanocoatings, Nanosystems, Nanotechnologies* (Oak Park, IL: Bentham Science Publishers) p 416
[37] Cavaleiro A and de Hosson J T M (ed) 2006 *Nanostructured Coatings* (New York: Springer) p 340
Cavaleiro A and de Hosson J T M 2011 *Nanostructured Coatings* (Moscow: Tekhnosfera) p 404
[38] Sandu C S, Medjani F, Sanjinés R, Karimi A and Lévy F 2006 *Surf. Coat. Technol.* **201** 4219–23
[39] Sandu C S, Medjani F and Sanjines R 2007 *Rev. Adv. Mater. Sci.* **15**(3) 173–8 (www.ipme.ru/e-journals/RAMS/no_31507/sandu.html)
[40] Dub S N and Novikov N V 2004 *J. Superhard Mater.* **6** 16–33
[41] Dub S N, Lim Y Y and Chaudhri M M 2010 *J. Appl. Phys.* **107** 043510